

Poly(catecholamine) Coated CsPbBr₃ Perovskite Microlasers: Lasing in Water and Biofunctionalization

Sangyeon Cho and Seok Hyun Yun*

Lead halide perovskite (LHP) is a promising material for various optoelectronic applications. Surface coating on particles is a common strategy to improve their functionality and environmental stability, but LHP is not amenable to most coating chemistries because of its intrinsic weakness against polar solvents. Here, a novel method of synthesizing LHP microlasers in a super-saturated polar solvent using sonochemistry and applying various functional coatings on individual microlasers in situ is described. Cesium lead bromine perovskite (CsPbBr₃) microcrystals, capped with organic polynorepinephrine (pNE) layers, are synthesized. The catechol group of pNE coordinates to bromine-deficient lead atoms, forming a defect-passivating and diffusion-blocking shell. The pNE layer enhances the material lifetime of CsPbBr₃ in water by 2000-fold, enabling bright luminescence and lasing from single microcrystals in water. Furthermore, the pNE shell permits biofunctionalization with proteins, small molecules, and lipid bilayers. Luminescence from CsPbBr₃ microcrystals is sustained in water over 1 h and observed in live cells. The functionalization method may enable new applications of LHP laser particles in water-rich environments.

The poor stability of LHPs in water is intimately related to their ionic nature. Unlike traditional inorganic semiconductors that require high-temperature epitaxial growth, LHPs are solution processable at room temperature. This low lattice energy inevitably leads to low stability in the polar environment. Appropriate encapsulation can protect LHP crystals from reactive molecules, enhancing device stability. Several post-synthetic methods have been demonstrated, such as atomic layer deposition (ALD) with amorphous alumina (AlO_x)^[13] or aluminum oxide (Al₂O₃)^[14] calcination with titanium dioxide (TiO₂)^[15] and sol-gel processes with silicon dioxides (SiO₂)^[16,17] or hydrophobic polymer,^[18–21] for embedding ensembles of LHP nanoparticles into a water-impermeable matrix. However, these methods have never been applied to encapsulate single individual particles. Recently, single LHP nanocrystals

have been successfully coated using in situ hydrolysis to form SiO₂ shells during ligand assisted reprecipitation (LARP).^[22] However, this method is not readily applicable to microcrystals because the capping ligands only create nanocrystallization due to slow crystallization rates^[23,24] and short reprecipitation time (within few seconds).^[25] Furthermore, the hydrolysis reaction causes partial dissolution of LHPs by polar reactants, resulting in compromised photoluminescence (PL) quantum yield and morphologies.^[26]


Herein, we report novel techniques that enable us to add various protective and functional materials on the surface of inorganic LHP microlasers. We use organic polynorepinephrine (pNE) for an initial coating on CsPbBr₃ microcrystals. The pNE polymer layer then allows us to conjugate various biological functional materials via spontaneous reactions at room temperature. We demonstrate core-shell LHP microparticles with two-fold improved quantum-yield and 2000-fold enhanced material lifetime in water. Functionalized LHP particles internalized by biological cells generate bright luminescence in the cytoplasm.

1. Introduction

Lead halide perovskite (LHP), such as CsPbBr₃ and CH₃NH₃PbBr₃, in the form of micro- and nanocrystals has emerged as an excellent semiconductor material for light-emitting diodes^[1,2] and photovoltaic devices.^[3] Furthermore, LHP can be used as a gain material for miniature lasers.^[4–9] The material gain up to 4000 cm⁻¹ was reported in bulk-like nanocrystals.^[10] Lasing from single LHP submicron crystals^[8,9] has been demonstrated with threshold pump fluences of 0.2–1 mJ cm⁻². Such miniaturized and efficient LHP lasers may have potential as life-science tools for cell tagging,^[11] intracellular sensing,^[12] and deep-tissue imaging,^[7] if they can be made stable in the aqueous environment and compatible with biological systems. However, thus far this possibility has been out of the question because of the extreme weakness of LHPs in water.

Dr. S. Cho, Prof. S. H. Yun
Wellman Center for Photomedicine
Massachusetts General Hospital and Harvard Medical School
Cambridge, MA 02139, USA
E-mail: syun@hms.harvard.edu

Dr. S. Cho, Prof. S. H. Yun
Harvard-MIT Health Sciences and Technology
Massachusetts Institute of Technology
Cambridge, MA 02139, USA

 The ORCID identification number(s) for the author(s) of this article can be found under <https://doi.org/10.1002/adfm.202101902>.

DOI: 10.1002/adfm.202101902

2. Results

2.1. One-Pot Synthesis of pNE-Coated CsPbBr₃ Microlasers

Figure 1a depicts the schematic of our novel core-shell particle synthesis based on sonochemical crystallization of the LHP core and subsequent polymerization of the pNE shell. First, CsBr (75 mM) and PbBr₂ salts (75 mM) are added into

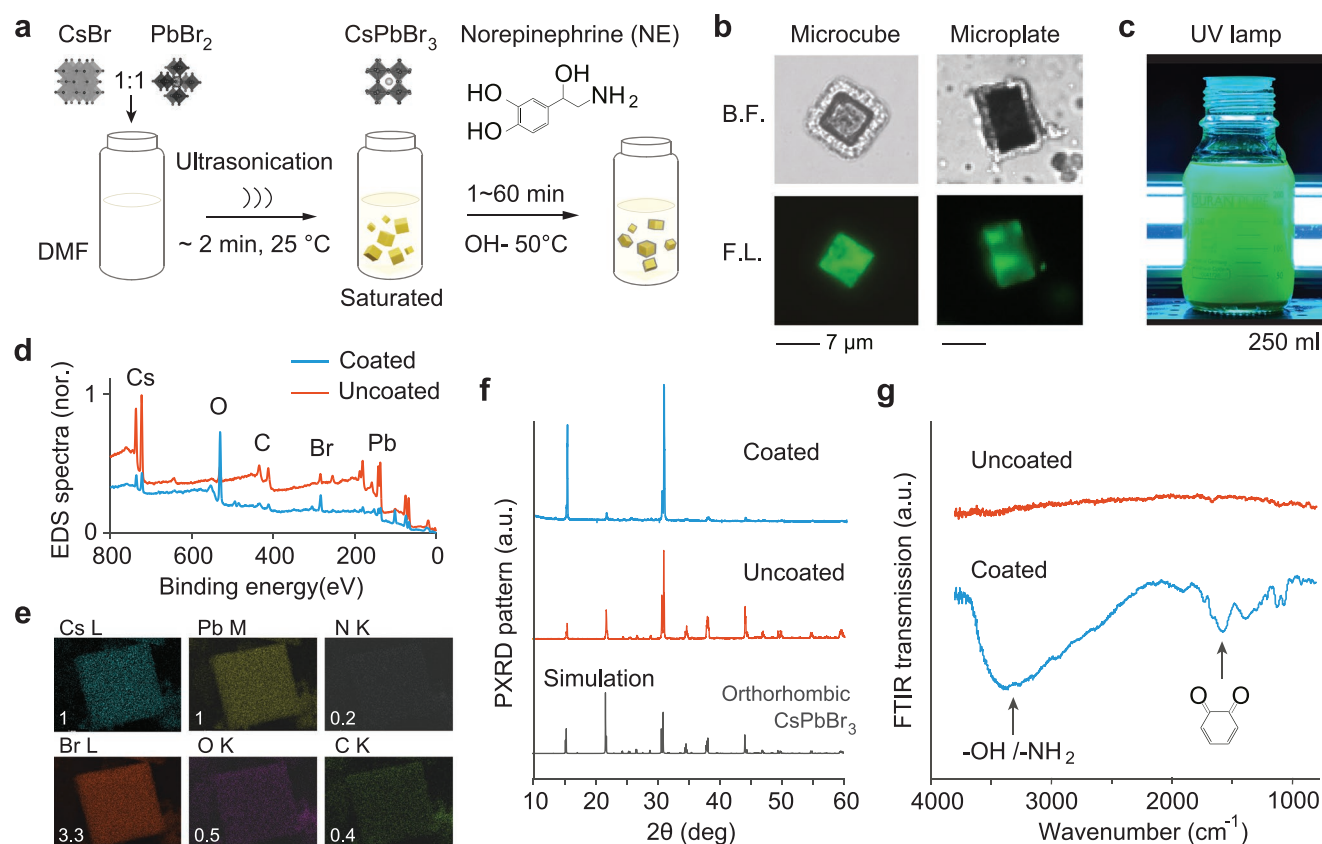


Figure 1. One-pot synthesis of core-shell CsPbBr₃-pNE microcrystals. a) Schematic of two reaction steps: Sonochemistry and polymerization of NE. b) Bright-field (top) and fluorescence (bottom) images of a pNE-coated CsPbBr₃ microcube (left) and microplate (right) in DMF immediately after coating. c) Core-shell particles in DMF under UV lamp. d) XPS spectra of microcrystals with and without pNE coating. e) Spatial elemental maps of a core-shell microparticle for the cesium L line, lead M line, bromine L line, nitrogen K line, carbon K line, and oxygen K line. Numbers are the measured stoichiometry ratio of the Cs, Pb, Br, N, C, and O content. f) Measured PXRD patterns of microcrystals with and without pNE coating, in comparison to a simulation result for the orthorhombic structure of CsPbBr₃ (space group Pbnm, a = 8.20 Å, b = 8.24 Å, c = 11.74 Å). g) Absorption spectra of uncoated and pNE-coated microparticles.

N,N-dimethylformamide (DMF) in room temperature. The PbBr₂ salts are partially dissolved in the DMF solution to produce Pb²⁺ and Br⁻ and the complexation^[27] of PbBr₃⁻ and PbBr₄²⁻. These ions react with undissolved CsBr salts and form a thin layer of orange-color CsPbBr₃ on their surface via fast interfacial reactions (Figure S1a, Supporting Information). Ultrasonication is applied to the mixture for about 2 mins using a bath- or tip-based ultrasonicator (Figure S1b, Supporting Information). Once ultrasonication starts, the remaining salts with interfacial CsPbBr₃ are broken into smaller pieces by ultrasonic forces and completely dissolved within 30–50 s. As the PbBr₄²⁻ concentration reaches a critical level over saturation, the nuclei of CsPbBr₃ are spontaneously formed at the vicinity of ultrasonic bubbles and grow to micro- and submicron crystals via: Cs⁺(sol) + PbBr₄²⁻(sol) → CsPbBr₃(s) + Br⁻(sol). The growth of microcrystals ceases after about 2 min of ultrasonication (Figure S1b, Supporting Information).

This one-pot synthesis is two-orders-of-magnitudes faster than the previous surface-initiated growth process^[28] that required ≈20 h to grow crystals to the size of a few μm. Scanning electron microscopy (SEM) of the CsPbBr₃ microcrystals showed cuboidal shapes without any noticeable cracked edges (Figure S1c,d, Supporting Information). The addition of a

nonionic surfactant, such as polysorbate 80, to the precursor solution resulted in an anisotropic growth of microplates and nanowires without perturbing supersaturation (Figure S1e).

Once the growth of CsPbBr₃ microcrystals is completed, they remain stable under the dynamic equilibrium in the saturated DMF solution. This opens up the opportunity to coat the surface by adding catecholamines. Poly-catecholamine coating, as found in mussel's sticky footage containing dihydroxyphenylalanine (DOPA) and tyrosine, is known for its ability to coat a wide range of materials.^[29,30] Following the sonochemical synthesis, we added 4 mg mL⁻¹ of a norepinephrine (NE) bitartrate salt and a pallet of sodium hydroxide (NaOH) into the solution (Figure 1a). After incubating at 50 °C for 1 h, pNE shells appear on the surface of the individual microcubes and microplates in the solution (Figure 1b). The solution maintains green fluorescence under ultra-violet (UV) light. It is possible to scale up the production of pNE-coated CsPbBr₃ particles simply by increasing the volume of the reactants (Figure 1c). Typically, we obtained about 10⁷ microcrystals per mL of DMF.

Energy-dispersive density spectroscopy (EDS), X-ray photoluminescence spectroscopy (XPS), and powder X-ray diffraction (PXRD) confirmed that the lattice sizes and stoichiometry of CsPbBr₃ after the coating were unchanged. The XPS

clearly shows the presence of the pNE shell (Figures 1d). The nitrogen-to-oxygen signal ratio (N/O) was measured to be ≈ 0.4 , close to the 0.33 ratio of the NE (Figure 1e). PXRD reveals the orthorhombic structure of single-crystalline CsPbBr₃ (space group Pbnm, A = 8.20 Å, B = 8.24 Å, C = 11.74 Å) (Figure 1f). Fourier-transform infrared (FTIR) spectroscopy showed absorption peaks at 3000–3500 cm⁻¹ corresponding to the amine and hydroxyl groups (Figure 1g). The characteristics absorbance peaks of the catechol and indole ring appeared at 1514 cm⁻¹ (Figure 1g). These functional groups offer binding sites to conjugate biomaterials via Schiff-base reactions and Michael additions.

2.2. Structural and Optical Characterization

SEM and transmission electron microscopy (TEM) images taken at different reaction times provided further insights into the coating process (Figure 2a). After 15 min of polymerization, a 25–60 nm thick, conformal shell appears unevenly on the surface. This morphology is consistent with our expectation that the NE molecules polymerize laterally via oxidative covalent linkage and grow vertically via π - π stacking and Pb²⁺-assisted coordination.^[30] The thickness of pNE shell was measured with samples titrated at different times during polymerization and

using TEM with 0.34 nm resolution (equivalent to accelerating voltage of 120 kV). Initially, the thickness of the conformal pNE shell increases linearly with incubation time, but after 30 min, it saturates at 40–80 nm depending on the crystallization direction (Figure 2b,c). The growth kinetics was analyzed using the sigmoidal equation.^[31] In the [010] direction, the maximum growth rate was 4.4 nm min⁻¹ and the thickness of the pNE layer after 30 min was 76 nm. In the [100] direction, the maximum growth rate was 2 nm min⁻¹, and the thickness was 41 nm. This asymmetry is attributed to the smaller steric hindrance at the regular octahedral site of the (010) surface compared to the tilted octahedral site of the (110) surface (Figure 2c, inset).

When the polymerization time exceeds 30 min, mesoporous pNE sheets appear outside the conformal pNE shell. SEM and TEM images present that the mesoporous pNE shell consists of multiple sheets grown along the surface normal (Figure 2a). Each sheet is 1 to 2 μ m in lateral size and contains numerous nanopores with 20 to 50 nm sizes and pNE aggregates with 3 to 8 nm in diameter (Figure S3, Supporting Information). We speculate that these colloidal pNE aggregates are stacked over time forming the supramolecular sheet structure. Under white-light illumination, the mesoporous pNE shell in saturated DMF solution appears transparent. However, when the saturated DMF was dried out, the mesoporous pNE became dark (light-absorbing)

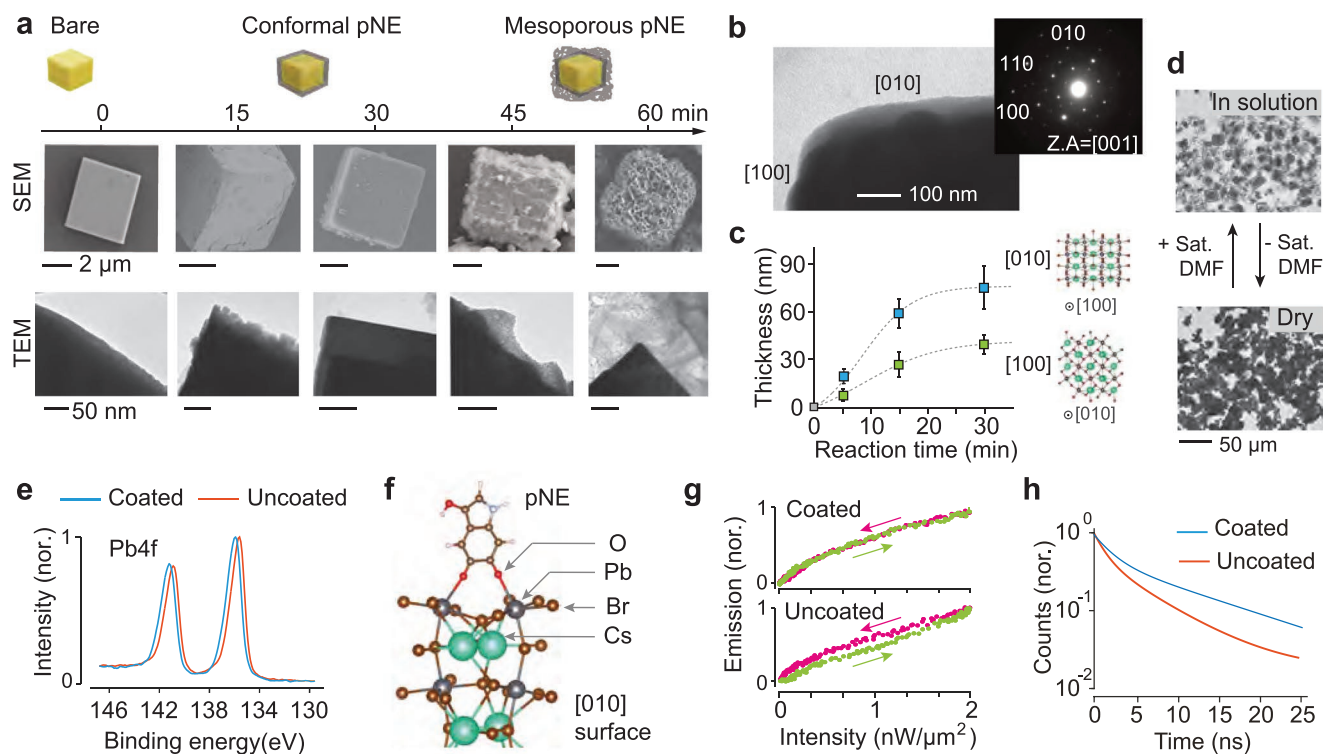


Figure 2. Structural and optical characterization. a) Time-lapse SEM and TEM images of different microparticles harvested at different reaction times, and schematic drawings of various reaction intermediates and final products. b) TEM image of the edge of conformal pNE coated CsPbBr₃. Corresponding selected area diffraction pattern in inset. c) Measured thickness of the thick and thin pNE layers at different reaction times. Error bars represent standard deviation measured with 15 samples. Dotted lines are sigmoidal fitting curves. Inset show the atomic structures of the two different planes. d) Optical transmission images of mesoporous pNE coated CsPbBr₃ with and without saturated DMF. e) High-resolution XPS of Pb4f in uncoated and pNE-coated samples. f) DFT-optimized structure of pNE bound on under-coordinated Pb atoms on the (010) surface of CsPbBr₃. g) PL curves of bare and coated CsPbBr₃ microparticles upon continuous-wave excitation at 491 nm. h) PL decay of bare and coated microparticles upon picosecond excitation at 382 nm.

(Figure 2d). Re-soaking the particles into saturated DMF solution recovers the transparency of the pNE shell. This reversible effect is due to the swelling property of the mesoporous pNE. DMF molecules intercalated into the pNE layers disrupt the pi–pi or cation–pi interactions and affect optical absorption^[32] and average refractive index^[33] of the pNE organogel. The light absorption of the dried pNE shell is responsible for a twofold decrease in PL intensity from CsPbBr₃, compared to the transparent pNE shell in the wet condition (Figure S2, Supporting Information).

High-resolution XPS showed that only 4f orbital electrons in the Pb atoms underwent a spectral blue-shift of 0.8 eV and also a broadening of 0.2 eV after coating (Figure 2e; and Figure S3, Supporting Information). This indicates that the electronegative catechol group with lone pair electrons binds to the electro-positive under-coordinated Pb atoms, forming Lewis acid-base adducts. A density functional theory (DFT) simulation suggests that two oxygen atoms in the catechol form a bidentate binuclear surface complex with the under-coordinated Pb atoms in the (010) surface (Figure 2f), as found in other catechol-metal oxides.^[34] The binding energy of pNE to the (010) surface (Figure S4a, Supporting Information) was calculated to be –0.13 eV, indicating that this process is thermodynamically favored. The DFT calculation of density of states suggests that the Lewis acid-base adduct can remove shallow trap states between the band edges (Figure S4b, Supporting Information).

To confirm this passivation effect, we measured photoluminescence (PL). After conformal pNE coating, the absolute PL quantum yield (η) of CsPbBr₃ microparticles increased from 1.5% to 2.9%, and the PL emission peak wavelength under picoseconds excitation at 390 nm was shifted from 531 to 525 nm (Figure S4c, Supporting Information). The blue-shift is attributed to the passivation of surface trap states,^[35–37] as supported in a DFT calculation (Figure S4b, Supporting Information). Under cyclic continuous-wave optical excitation, the PL intensity of uncoated CsPbBr₃ showed hysteresis due to the filling and saturation of carrier trap states.^[36] The hysteresis was nearly eliminated after coating (Figure 2g). The measured transient PL decay curves (Figure 2h) were fitted to a double-exponential model (Table S1, Supporting Information) with two lifetime constants, τ_1 and τ_2 , accounting for fast carrier quenching through trap states and slow radiative recombination, respectively.^[38] Coated CsPbBr₃ particles exhibited τ_1 of 2 ns and τ_2 of 12.2 ns, about twofold increase compared to uncoated CsPbBr₃ with τ_1 of 1.3 ns and τ_2 of 6.2 ns. Cyclic voltammetry (Figure S5, Supporting Information) further confirmed the passivation effect of pNE.

2.3. Enhanced Material Stability and Lasing in Water

Material stability against water was dramatically improved after pNE coating (Figure 3a). When immersed in water, uncoated CsPbBr₃ microparticles dissolve immediately (<0.3 s). By contrast, coated CsPbBr₃ microparticles maintained optical absorbance and green fluorescence in water for \approx 10 min. This 2000-fold enhanced material lifetime enabled us to observe lasing from single core-shell microparticles in water upon optical pumping (480 nm, pulse width: 5 ns) (Figure 3b; and Figure S6, Supporting Information). The far-field emission pattern of a core-shell CsPbBr₃ particle with a size of 4 μ m showed

uniform fluorescence below lasing threshold and bright scattering spots above threshold (Figure 3c; see Figure S7, Supporting Information, for a 1.5- μ m-sized particle and Figure S7b, Supporting Information, for a 6- μ m-sized particle). A narrowband lasing peak at 537 nm is evident, superimposed on a broad fluorescence background (Figure 3d). This laser particle showed a light-in-light-out (L–L) curve with a pump threshold of 0.85 mJ cm^{–2}, 3.4 folds higher than the threshold fluence in the air ($n = 1$) due to the higher refractive index ($n = 1.33$) of the water (Figure S7c, Supporting Information). The linewidth narrowing near the threshold is another evidence of lasing (Figure 3e). The narrowest linewidth near the threshold was \approx 0.5 nm in FWHM. Lasing in water lasted for about 100 pump pulses at a fluence of 1 mJ cm^{–2}. Over repeated lasing actions, the microcrystals gradually lose PL efficiency. This accelerated photodamage of CsPbBr₃ by photoexcitation and lasing action in water indicates that photochemical reactions occur between CsPbBr₃ and hydronium (H₃O⁺) or hydroxide (OH[–]) ions at the interface.^[39] Detail of this effect is not fully understood and a subject of investigation.

2.4. Lasing from Submicron-Sized Core-Shell CsPbBr₃ Particle in Air

We measured the threshold pump laser fluence for a large number of CsPbBr₃ particles with different sizes in the ambient air (Figure 3f) and found that the pNE coating allowed substantially smaller CsPbBr₃ microcrystals to reach lasing threshold, compared to uncoated CsPbBr₃ particles. The smallest lasing particle we observed had a cuboidal shape with a length of 850 nm including the 50-nm thick pNE layers in all sides (Figure 3g). This particle showed a typical nonlinear light-in-light-out curve with a lasing threshold pump fluence of 0.8 mJ cm^{–2} (Figure S8a, Supporting Information). The output spectra (Figure 3h) showed single mode oscillation at 537 nm. The linewidth of the laser mode was \approx 0.5 nm. A finite-difference-time-domain (FDTD) simulation estimates that the cavity mode has a radiative Q-factor of \approx 1000 (Figure 3g; and Figure S8b, Supporting Information) and an absorptive Q-factor of \approx 480 assuming a material absorption coefficient of 600 cm^{–1}.^[9] To achieve a net positive gain for lasing, the particle should have a net gain coefficient larger than 320 cm^{–1}. This value is comparable to those of perovskite films,^[40] III–V semiconductors,^[41] and II–VI semiconductors.^[42] The pulse-to-pulse intensity variation from the core-shell particles (Figure 3i) was 6 times smaller than uncoated particles.^[43] The output intensity of coated particles (15 samples) decreased exponentially with a decay constant of \approx 18 000 pulses and was stabilized to a 60% level of the pristine value and the lasing peak wavelength was stable with a standard deviation of 0.08 nm. This is comparing to the uncoated particles with 0.47 nm of pulse-to-pulse instability and greater intensity decay.^[43] These enhanced lasing characteristics are due to the defect passivation by pNE coating.

2.5. Biofunctionalization

The considerable lifetime (>5 min) of core-shell laser particles in water allow many spontaneous chemical reactions to be

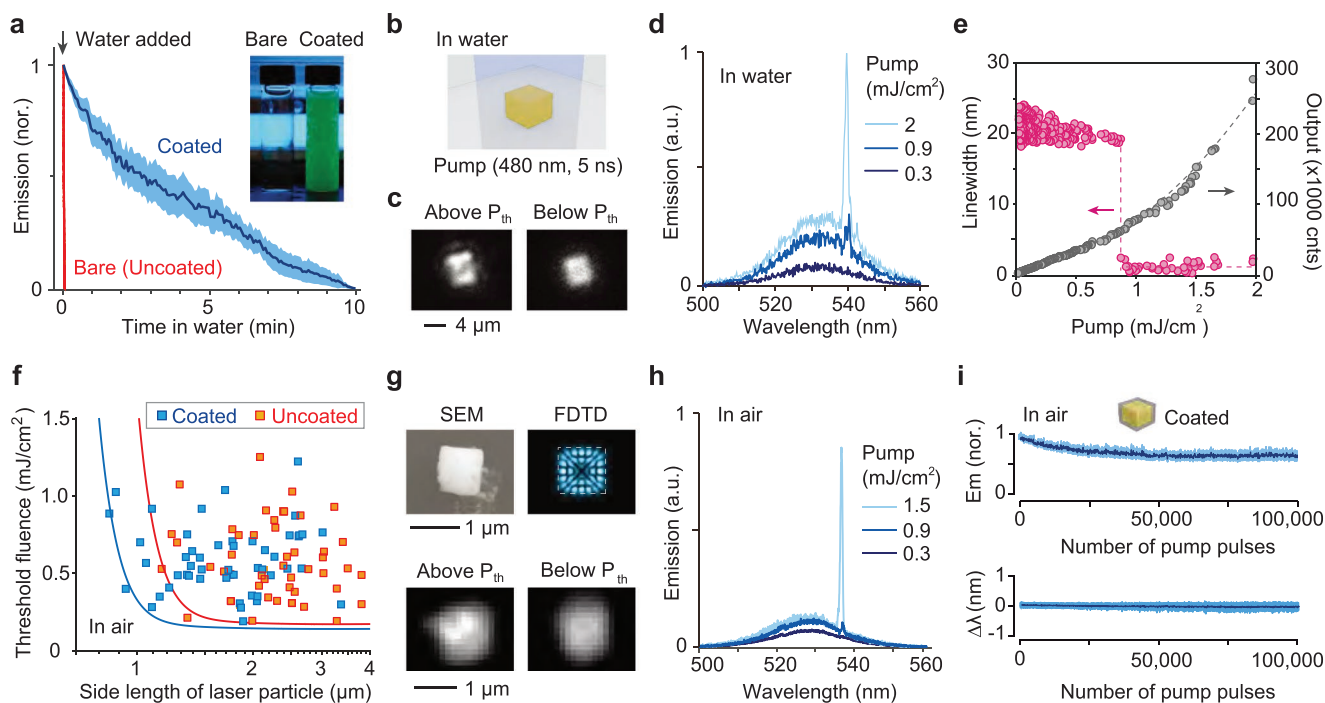


Figure 3. Lasing in water and air. a) Stability of uncoated and pNE-coated CsPbBr₃ microcrystals in water. The shaded region represents standard deviation of 15 different particles. b) Schematic of optical pumping. c) Emission spectra of a microparticle in water at two different pump fluences. d) Measured spectral linewidth and light-in-light-out curve of a laser particle in water at different pump fluences. A dramatic linewidth reduction occurs at the lasing threshold fluence of 0.85 mJ cm⁻². e) Emission intensity patterns below and above the threshold for a pNE-coated CsPbBr₃ microcrystal in water. f) Measured lasing threshold and length of various uncoated (orange) and pNE-coated (blue) CsPbBr₃ particles in air. Solid curves: theoretical estimations. g) (top, left) SEM image of the smallest lasing core-shell particle with a length of 850 nm, (top, right) finite-difference time domain (FDTD) simulation, (bottom) wide-field fluorescence images above and below its lasing threshold at 0.8 mJ cm⁻². h) Output spectra from the submicron laser particle at different pump levels: 0.3, 0.9, 1.5 mJ cm⁻² (pulse duration: 5 ns, pump wavelength: 480 nm). i) Variation of laser output intensity and wavelength of coated CsPbBr₃ particles (15 samples) over 100 000 pump pulses (20 Hz, at fluence twice the lasing threshold of each particle). Dark blue lines: mean values, shaded regions: 95% confidence intervals.

used for surface functionalization. We performed four different proof-of-concept experiments to demonstrate functionalization with biomolecules.

First, we encapsulated core-shell perovskite particles with lipid bilayers (Figure 4a). For this, we prepared 1- μ m-size large unilamellar vesicles (LUVs) made of DIR dye-labeled, 1,2-dioleoyl-sn-glycero-3-phosphoethanolamine (DOPE) and 1,2-dioleoyl-3-trimethylammonium-propane (DOTAP) using a conventional extrusion method.^[44] When mixed with pNE-coated particles in water, LUVs are deposited on the surface of the pNE via direct vesicle fusion (Figure 4b, inset). The lipid bilayer was removed from the particles by chloroform solvent, which suggests that LUVs interact with pNE via non-covalent bonding (Figure S9a, Supporting Information). The structural and optical properties of the CsPbBr₃ core are intact after functionalization, evidenced by preserved cube-shapes and lasing in water (Figure S9b,c, Supporting Information). The lipid bilayer-functionalized core-shell CsPbBr₃ microparticles produced PL for over 1 h in water (Figure 4b). Further improved stability enabled us to deliver the lipid-coated particles to the cytoplasm of 4T1 breast cancer cells in vitro (Figure 4c). Upon excitation, distinct green fluorescence is generated from the particles in the cytoplasm. To evaluate the cytotoxic effect, we performed a CCK assay with 4T1 mouse breast tumor cells after incubation over 24 h with different

concentrations of lipid-coated particles. The cell viability (120%) for the sample incubated with 0.28 μ g mL⁻¹, for which the particle-to-cell ratio is approximately 1:1, showed mild toxicity compared to the cell viability (150%) of control samples (P value < 0.01). This implies that releasing of heavy metal ions (Pb²⁺) affects cellular mitotic processes and homeostasis. The lethal concentration 50 (LC50) by linear regression was measured to be 0.96 μ g mL⁻¹ by linear regression. Therefore, the concentration (0.28 μ g mL⁻¹) of one intracellular microlaser per cell would be acceptable for most short-term in vitro experiments.

Second, we conjugated biotin-dPEG₂₃-NH₂ to the pNE shell using Schiff-base reaction (Figure 4d). The biotinylated LHP particles are firmly anchored on a streptavidin-coated plate (Figure 4e). Under a strong pump fluence (2 mJ cm⁻²), the optical radiation force moves non-biotinylated particles,^[45] but biotinylated particles remain stationary (Figure 4f).

Third, we functionalized core-shell LHP particles with fluorescent proteins (Figure 4g). DsRed fluorescent proteins (RFPs) in the phosphate buffered saline (PBS) were mixed with pNE-coated CsPbBr₃ particles in ethanol with 1:1 volume ratio. The mixture was incubated for 5 min for the RFPs to attach to the pNE via Schiff-base reaction. Fluorescence spectroscopy (Figure 4h) and imaging (Figure 4i) confirmed the presence of RFP on the surface of the microparticles. The gradual

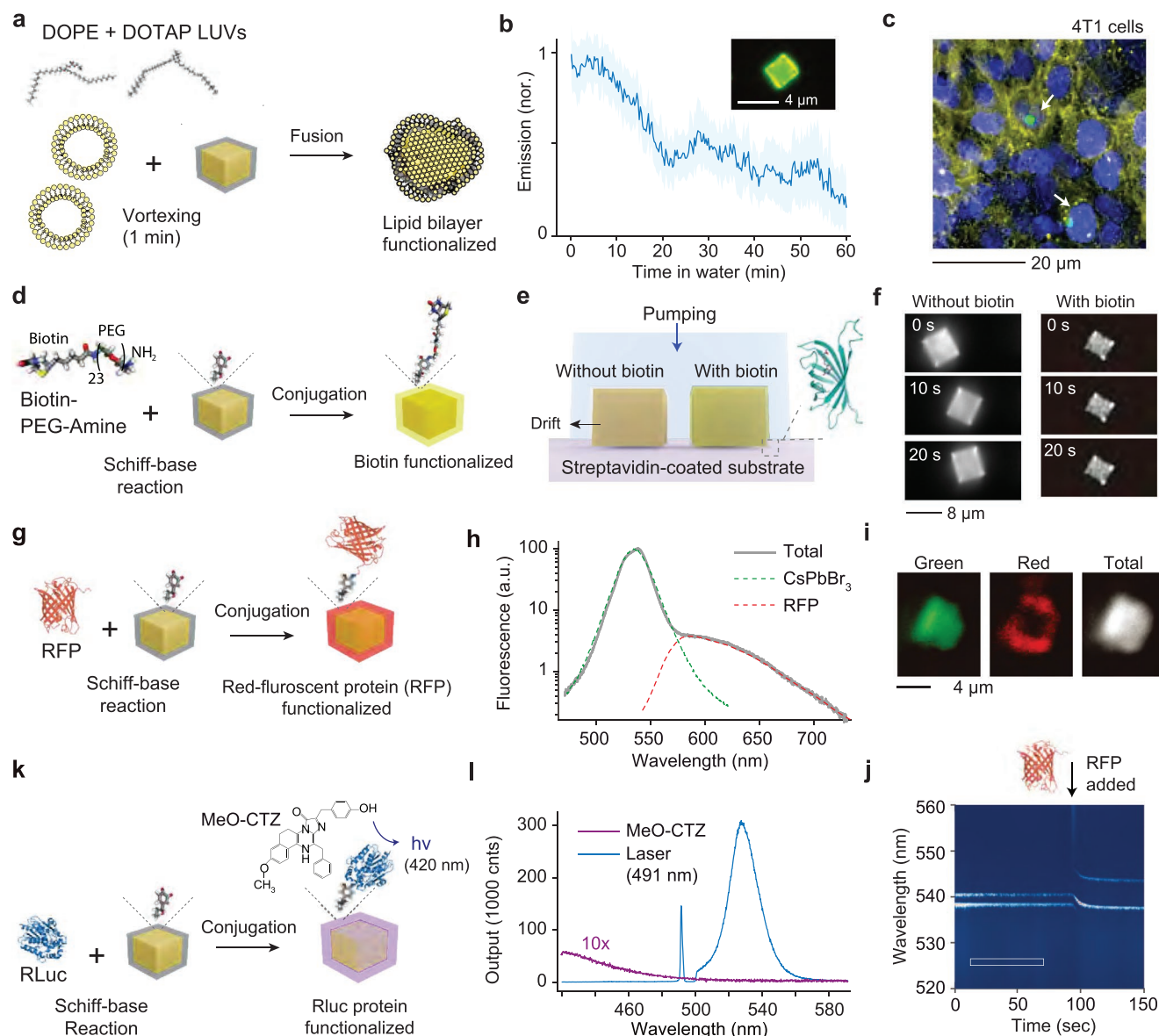


Figure 4. Biofunctionalization. a) Schematic of lipid–bilayer functionalization. b) Stability of lipid-coated microcrystals in water. The shaded region depicts the standard deviation of 15 different particles. Inset, image of a single microcube in water emitting green fluorescence from CsPbBr₃ and infrared fluorescence from DIR dye (rendered in yellow) conjugated to the lipid-bilayers. c) Fluorescence image showing the nuclei (DAPI, blue) of 4T1 tumor cells, lipid bilayers (DIR, yellow), and core-shell particles (CsPbBr₃, green). d) Schematic of biotinylation using biotin-dPEG₂₀-NH₂. e) Schematic of lasing experiment of bare and biotin-functionalized microparticles on the streptavidin coated substrate. f) Time-lapse images showing the immobilization of biotinylated particle due to biotin–streptavidin interaction. g) Schematic of RFP conjugation. h) Emission spectra from a CsPbBr₃-RFP conjugate particle. i) Fluorescence images of an RFP-coated particle. j) Time-lapse spectroscopy of 1.8 μm-sized laser particle in ethanol. The addition of RFP (10 μM) at 94 s causes a shift of the laser emission wavelength. k) Schematic of bioluminescence protein (RLuc) conjugation. l) Emission spectra from a single RLuc-coated particle. Purple curve: when mixed with MeO–CTZ (in PBS buffer), blue curve: under laser excitation at 491 nm at 1 μW μm⁻². The peak at 491 nm is due to residual pump light through a dichroic filter.

binding of RFP is evident in the spectral shift of the laser peak and the increase of RFP emission (Figure 4j; and Figure S11, Supporting Information). It is noteworthy that partial anion exchange chemistry can tune the fluorescence color of LHP particles via solid-state halide diffusion.^[46] The LHP-protein hybrid microparticles have potential for biological applications such as multiplexed assay,^[47] single molecule biophysics,^[48] and hyperspectral imaging.^[49]

Last, we attached bioluminescent Renilla luciferase-8 (Rluc8) on the surface of particles (Figure 4k). Rluc8-coated hybrid particles (a mean size of 4 μm) on a glass substrate produce bioluminescence centered at 420 nm (Figure 4l) when 10 μl PBS solution of 50 μM of C6-methoxyphenylcoelenterazine (MeO–CTZ) was applied. When excited with continuous-wave laser at 491 nm, the hybrid particles showed bright green fluorescence of CsPbBr₃ (Figure 4l).

It is possible to attach a variety of other functional materials, such as alkanethiol molecules for hydrophobic functionalization in organic solvents (Figure S12, Supporting Information), plasmonic nanoparticles for local-field enhancement, and conductive polymers for charge-transfer coupled redox sensor to pNE coated microparticles. As alternatives to polycatechol, self-polymerizable polyethyleneimine^[50] with multiple nitrogen atoms and polyphenol coating^[51] may be used for the coating of LHP particles.

3. Conclusion

In summary, we have demonstrated facile large-scale sonochemical synthesis, passivating coating, and functionalization of core-shell-type CsPbBr₃ microlasers. The pNE shell and functionalization extended the lifetime of CsPbBr₃ microparticles in water significantly, enabling us to achieve stable lasing from single core-shell CsPbBr₃ microparticles in water. The functionalized LHP microlasers may open new possibilities for applications with biological samples.

4. Experimental Section

Materials and Reagents: CsBr (99.99%), PbBr₂ (99.99%), NaOH (Pallets), (±)-Norepinephrine (+)-bitartrate salt, *N,N*-Dimethylformamide (anhydrous, 99.8%), ethanol (anhydrous, ≥99.5%) were purchased from Sigma–Aldrich. 1,2-dioleoyl-sn-glycero-3-phosphoethanolamine (DOPE) and 1,2-dioleoyl-3-trimethylammonium-propane (DOTAP) were purchased from Avanti polar lipid. DiI_{C18}(7) (1,1'-Dioctadecyl-3,3',3'-Tetramethylindotricarbocyanine Iodide) dye (DIR), proLong gold antifade mountant with 4',6-diamidino-2-phenylindole (DAPI), and streptavidin-coated 96 well plates were purchased from Thermo Scientific. Biotin-dPEG₂₃-NH₂ was purchased from Quanta Biosdesign. Phosphate Buffered Saline (PBS, pH = 7.4) was purchased from Invitrogen/Gibco. rDSRed-express protein was purchased from Takara Bio. MeO-eCTZ was purchased from Nanolight and RLuc8 (in PBS, pH 7.4) was purchased from G-Biosciences. All reagents were used as received without further purification.

Synthesis of Core-Shell CsPbBr₃-pNE Microcrystals: Sonochemical synthesis of core CsPbBr₃ microcrystals. CsBr and PbBr₂ were dispersed at an equal concentration in 1 mL of *N,N*-dimethylformamide (DMF) in a vial. The typical concentration of the precursor salts was 0.075 M each. The vial was then placed into a bath-type ultrasonicator (Elmasonic P60H, Elma) or a single step tip ultrasonicator (Fisherbrand Q125) in room temperature and irradiated with ultrasonic waves at a frequency of 20–80 kHz. After 2–3 min of ultrasonication, single-phase CsPbBr₃ microcrystals were spontaneously crystallized and colloiddally dispersed in the solution. Sonochemically synthesized LHPs microparticles stay stable in DMF due to supersaturation and can undergo pNE coating. 4 mg of (±)-Norepinephrine (+)-bitartrate salt and a pallet of NaOH were mixed with the solution and vortexed for 3 s. Undissolved NaOH pallet was discarded. The vial with untightened cap was shaken at 800 rpm in 50 °C for ≈20–30 min to construct conformal pNE coating, and for 1 h to form mesoporous pNE coating. The product was centrifuged at 4000 rpm for 2 min and the remaining precursors were washed several times with ethanol. Finally, the core-shell particles were stored in ethanol for further use.

Bifunctionalization: For perovskite-lipid-bilayer hybrid, first, the large unilamellar vesicles (LUVs) consisting of DOPE and DOTAP were synthesized by using conventional extrusion method.^[44] Prepared LUVs in water were stained with DIR dye for near-infrared fluorescence imaging. For lipid-bilayer coating, the LUVs were mixed with pNE-coated CsPbBr₃ particles in ethanol in a 1:1 vol/vol ratio and then vortexed for 1 min for sufficient encapsulations. For cell experiments,

the lipid-coated particles (concentration: 0.28 μg mL⁻¹) were added to living 4T1 breast cancer cells and the cells were incubated at 37 °C and 5% CO₂ for 10 min. After delivering process, cells were stained after fixation with DAPI for nucleus and imaged under the fluorescence and bright-field microscopy to confirm particle uptake (Keyence BZ-X700 microscope). For biotinylated perovskite particles, pNE-coated CsPbBr₃ in ethanol was mixed with 6 mg of biotin-dPEG₂₃-NH₂ and then incubated at room-temperature for 1 h. After the biotinylation, the product was washed two times with ethanol. For tethering experiments, the prepared particles were drop-casted to the streptavidin-coated 96 well plate and dried-out the ethanol solvent using N₂ flows. For perovskite-RFP hybrid, pNE-coated CsPbBr₃ was mixed in PBS buffer containing rDSRed-express protein (100 μg 1 mL⁻¹). After incubation for 5 min, the product was centrifuged at 8000 rpm for 5 min and then the supernatant was removed. The product was washed two times with fresh PBS to remove unattached proteins. The perovskite-RFP hybrid was re-dispersed in fresh PBS buffer and immediately transferred to a glass substrate for optical characterization. For perovskite-RLuc hybrid, pNE-coated CsPbBr₃ was mixed in PBS buffer containing RLuc8 protein (5 mg 1 mL⁻¹). After incubation for 5 min, the product was centrifuged at 8000 rpm for 5 min and then the supernatant was removed. The product was washed two times with fresh PBS to remove unattached proteins. The final product was drop-casted on the glass substrate. For generating bioluminescence, MeO-CTZ (50 μM in PBS buffer) was mixed with the product solution on the substrate.

In Vitro Cytotoxicity Assays: 4T1 mouse breast tumor cells (source: ATCC) were cultured and maintained in serum-supplemented cell media following the manufacturer's guidelines. The cells were seeded on a 96-well plate (1 × 10⁴ cells per well) with 150 mL of HDMEM (Gibco) supplemented with 10% (v/v) fetal bovine serum (FBS) and 1% (v/v) penicillin-streptomycin, and incubated at 37 °C and 5% CO₂. After culturing for 24 h, the cell culture medium was replaced with 150 mL of fresh HDMEM whole cell medium containing different concentrations of LPs (from 0 to 1.1 μg mL⁻¹). After co-culturing for another 24 h, the cell culture medium with LPs was removed and CCK-8 medium added (no FBS) to quantitatively evaluate the cell viability. The absorbance at 450 nm was measured on a microplate spectrophotometer as an indicator of viable cells. The cell viability was normalized to the control group (non-treatment).

Material Characterization: For SEM and EDX measurements, samples were transferred onto a chipped Si wafer by drop casting and imaged using a Zeiss Merlin high-resolution SEM equipped with an EDX detector operated at 15 kV. For TEM measurements, samples were prepared by drop casting microparticles onto TEM grids (Ted Pella). TEM images were acquired using a FEI Tecnai Multipurpose TEM operated at 120 kV. The illumination beam was expanded to avoid sample damage. For power X-ray diffraction (PXRD) measurements, PXRD patterns over 2θ angles from 10° to 60° were collected using a PANalytical X'Pert PRO high-resolution X-ray diffraction system with a CuKα irradiation source. These measurements were performed at the MIT Center for Material Science and Engineering (CMSE). For XPS measurements, the spectrum was collected using a physical Electronics Versaprobe II with monochromated Al (1486.6 eV) irradiation source having a beam size of 200 μm. The survey analysis was conducted with step sizes of 0.8 eV and a digital pass energy of 182.8 eV. The high energy resolution scan of the Cs3d, Pb4f, Br3p, Cl1s, and O1s regions was taken with step sizes of 0.1 eV and the digital pass energy of 23.5 eV. For FTIR spectroscopy measurements, the reflection spectrum from the sample on a chipped Si wafer was measured using a Thermo Fisher 6700 FTIR Bench. These measurements were performed at the MIT center for material science and engineering (CMSE).

Optical Characterization: Optical absorbance spectra were measured using a spectrophotometer (BioTek, Epoch2). Widefield brightfield and fluorescence images were obtained using an optical microscope (Keyence, BZ-X). For time-resolved photoluminescence measurements, a picosecond laser (VisIR-765, PicoQuant) was used, which was frequency-doubled to 382 nm using a nonlinear BBO crystal (Figure S20, Supporting Information), a single-photon avalanche photodiode (Micro Photonics Devices) with a response time of 50 ps, and a time-correlated

single-photon counting board (TimeHarp 260, PicoQuant) with a resolution of 25 ps. For absolute quantum yield measurements, a vial of colloidal dispersed LHPs microcrystals in solution was placed in an integrating sphere (Thorlabs) and excited using the 382-nm frequency-doubled picosecond laser. The spectra of light collected from the integrating sphere was coupled, via a multimode fiber, to a spectrometer (Shamrock, Andor) consisting of a diffraction grating and an electron multiplier charge-coupled device (EMCCD) camera. For lasing experiments in water, LHPs microcrystals were centrifuged at 8000 rpm for 2 min and the supernatant removed. The particles were mixed with pure water and vortexed for 30 s for uniform dispersion. The particle solution was transferred onto a standard 35 mm glass-bottom dish. The specimen was placed in a home-built epi-fluorescence microscopy setup (Figure S6, Supporting Information). The pump source was an optical parametric oscillator (OPO, Optotek HE 355 LD) tuned to 480 nm and circularly polarized, with a repetition rate of 20 kHz and a pulse duration of 4 ns. Using a 0.6 NA, 50x air objective lens (Nikon), the full-width-at-half-maxima (FWHM) size of the pump beam on the sample was adjusted to $\approx 38 \mu\text{m}$. The emission from the sample collected by the objective lens was passed through a dichroic mirror and a dichroic filter and split to an EMCCD camera (Luca, Andor) for wide-field imaging and to the grating-based EMCCD spectrometer (Shamrock, Andor). With an entrance slit width of $20 \mu\text{m}$, the measurement spectral resolution was $\approx 0.13 \text{ nm}$. For real-time observation of RFP attachment, the $10 \mu\text{L}$ of 5 nm pNE-coated perovskite particles in ethanol were transferred onto a standard 35 mm glass-bottom dish and the ethanol dried out using N_2 flow. Then additional 3 mL of ethanol was added to the dish. Under nanoseconds optical pumping at 20 Hz and single-shot acquisition using external triggering, the spectra was recorded during the addition of $1 \mu\text{L}$ of RFP solution on the top of the surface of the ethanol solution in the dish. As an excitation source for photoluminescence analysis, a continuous-wave, diode-pumped laser (491 nm, Cobolt Calypso) was used. All measurements were conducted at room temperature.

Density Functional Theory (DFT) Calculation: First principle calculations were carried out using the quantum espresso package, a density functional theory (DFT) approach. The electron-ion interactions described by standard-solid-state-pseudopotentials (SSSP) with electrons from Cs 6s, 5p, 5d; Pb 6s, 6p, 5d; Br 4s 4p; C, N and O 2s, 2p; and H 1s shells were included in the calculations. The Perdew-Burke-Ernzerhof (PBE) version of the generalized gradient approximation (GGA) was adopted for exchange correlation. The energy cutoff of 30 and 180 Rydberg was adopted for wavefunctions and charge density expansion, respectively. The k-point mesh $3 \times 3 \times 1$ was used for orthorhombic CsPbBr_3 unit cell and surface structure calculations, respectively. Surface slabs were modeled as PbBr_2 -terminated slabs, which had 9 layers of CsBr and PbBr_2 in total. 15 \AA vacuum was added on top of the slab surface to minimize the interaction between the adjacent slabs. In all electronic structure calculations, the self-consistent field (SCF) was terminated when the estimated energy error was $< 10^{-4}$ Rydberg. All crystal structures were relaxed to their lowest energy structures using Broyden-Fletcher-Goldfarb-Shanno minimization (BFGS).

Electrochemical Bandgap Characterization: Fluorine doped tin oxide (FTO) substrates were rinsed with DI water and acetone and dried out prior to use. LHPs microparticles were transferred onto fluorine doped tin oxide (FTO) glass electrodes by drop-casting. Dichloromethane (DCM) was used as the solvent. The conducting electrolytes were 0.1 M of tetrabutylammonium tetrafluoroborate (TBAF_4). The FTO/perovskite electrodes functioned as the working electrode, a Pt mesh (1 cm^2) as the counterelectrode, and homemade Ag/AgCl wire (an Ag wire having AgCl deposited on its surface) as the pseudoreference electrode. Cyclic voltammetry (CV) measurements using a Biologic VSP 16-channel potentiostat and a three-electrode electrochemical cell with a porous glass frit separating the counter electrode from the working and reference electrodes were carried out. The thermodynamic potential of the electrodes was measured dissolving an amount of ferrocene into the solution.

Finite-Difference Time-Domain (FDTD) Simulation: FDTD simulations for 850 nm perovskite core-shell resonators (core material: CsPbBr_3 ($n = 2.5$), core dimension: $750 \text{ nm} \times 750 \text{ nm} \times 600 \text{ nm}$, shell material:

pNE ($n = 1.51$), shell thickness: 50 nm) on a glass substrate in air were performed using commercial software (Lumerical). The extremely fine mesh was set around the cube (size 5 nm). The time apodization was centered at 450 fs with time width of 100 fs.

Supporting Information

Supporting Information is available from the Wiley Online Library or from the author.

Acknowledgements

The authors thank Dr. Hao Yan for performing CCK assay and helping in the cell experiments and Dr. Soyoung Kim and Prof. Surendranath at MIT for helping electrochemical characterizations. This research was supported in part by the Massachusetts General Hospital Research Scholar Award and National Institutes of Health (grant no. DP1EB024242). S.C. acknowledges the Bullock-Wellman fellowship and the Samsung Scholarship. Part of this work used the facilities in the Center for Materials Science and Engineering at MIT.

Conflict of Interest

The authors declare no conflict of interest.

Data Availability Statement

Research data are not shared.

Keywords

biofunctionalization, core-shell, lead halide perovskites, microlasers

Received: February 23, 2021

Revised: March 25, 2021

Published online: April 25, 2021

- [1] H. Cho, S.-H. Jeong, M.-H. Park, Y.-H. Kim, C. Wolf, C.-L. Lee, J. H. Heo, A. Sadhanala, N. Myoung, S. Yoo, *Science* **2015**, 350, 1222.
- [2] Y. Cao, N. Wang, H. Tian, J. Guo, Y. Wei, H. Chen, Y. Miao, W. Zou, K. Pan, Y. He, *Nature* **2018**, 562, 249.
- [3] M. A. Green, A. Ho-Baillie, H. J. Snaith, *Nat. Photonics* **2014**, 8, 506.
- [4] G. Xing, N. Mathews, S. S. Lim, N. Yantara, X. Liu, D. Sabba, M. Grätzel, S. Mhaisalkar, T. C. Sum, *Nat. Mater.* **2014**, 13, 476.
- [5] Y. Jia, R. A. Kerner, A. J. Grede, B. P. Rand, N. C. Giebink, *Nat. Photonics* **2017**, 11, 784.
- [6] H. Zhu, Y. Fu, F. Meng, X. Wu, Z. Gong, Q. Ding, M. V. Gustafsson, M. T. Trinh, S. Jin, X. Y. Zhu, *Nat. Mater.* **2015**, 14, 636.
- [7] S. Cho, M. Humar, N. Martino, S. H. Yun, *Phys. Rev. Lett.* **2016**, 117, 193902.
- [8] E. Tiguntseva, K. Koshelev, A. Furasova, P. Tonkaev, V. Mikhailovskii, E. V. Ushakova, D. G. Baranov, T. Shegai, A. A. Zakhidov, Y. Kivshar, *ACS Nano* **2020**, 14, 8149.
- [9] S. Cho, Y. Yang, M. Soljačić, S. H. Yun, (Preprint) arXiv:2007.09265v1, July 2020.
- [10] P. Geiregat, J. Maes, K. Chen, E. Drijvers, J. De Roo, J. M. Hodgkiss, Z. Hens, *ACS Nano* **2018**, 12, 10178.

- [11] N. Martino, S. J. J. Kwok, A. C. Liapis, S. Forward, H. Jang, H.-M. Kim, S. J. Wu, J. Wu, P. H. Dannenberg, S.-J. Jang, Y.-H. Lee, S.-H. Yun, *Nat. Photonics* **2019**, *13*, 720.
- [12] M. Schubert, L. Woolfson, I. R. M. Barnard, A. M. Dorward, B. Casement, A. Morton, G. B. Robertson, P. L. Appleton, G. B. Miles, C. S. Tucker, *Nat. Photonics* **2020**, *14*, 452.
- [13] A. Lojudice, S. Saris, E. Oveisi, D. T. L. Alexander, R. Buonsanti, *Angew. Chem., Int. Ed.* **2017**, *56*, 10696.
- [14] H. Yu, X. Xu, H. Liu, Y. Wan, X. Cheng, J. Chen, Y. Ye, L. Dai, *ACS Nano* **2019**, *14*, 552.
- [15] Z. Li, E. Hofman, J. Li, A. H. Davis, C. Tung, L. Wu, W. Zheng, *Adv. Funct. Mater.* **2018**, *28*, 1704288.
- [16] Z. Hu, Z. Liu, Y. Bian, S. Li, X. Tang, J. Du, Z. Zang, M. Zhou, W. Hu, Y. Tian, *Adv. Opt. Mater.* **2018**, *6*, 1700997.
- [17] S. Huang, Z. Li, L. Kong, N. Zhu, A. Shan, L. Li, *J. Am. Chem. Soc.* **2016**, *138*, 5749.
- [18] P. G. Papagiorgis, A. Manoli, A. Alexiou, P. Karacosta, X. Karagiorgis, G. Papaparaska, C. Bernasconi, M. I. Bodnarchuk, M. V. Kovalenko, T. Krasia-Christoforou, *Front. Chem.* **2019**, *7*, 87.
- [19] H. Huang, B. Chen, Z. Wang, T. F. Hung, A. S. Sussha, H. Zhong, A. L. Rogach, *Chem. Sci.* **2016**, *7*, 5699.
- [20] M. Gong, R. Sakidja, R. Goul, D. Ewing, M. Casper, A. Stramel, A. Elliot, J. Z. Wu, *ACS Nano* **2019**, *13*, 3714.
- [21] H. Wu, S. Wang, F. Cao, J. Zhou, Q. Wu, H. Wang, X. Li, L. Yin, X. Yang, *Chem. Mater.* **2019**, *31*, 1936.
- [22] Q. Zhong, M. Cao, H. Hu, D. Yang, M. Chen, P. Li, L. Wu, Q. Zhang, *ACS Nano* **2018**, *12*, 8579.
- [23] A. Pan, B. He, X. Fan, Z. Liu, J. J. Urban, A. P. Alivisatos, L. He, Y. Liu, *ACS Nano* **2016**, *10*, 7943.
- [24] S. Sun, D. Yuan, Y. Xu, A. Wang, Z. Deng, *ACS Nano* **2016**, *10*, 3648.
- [25] H. Huang, J. Raith, S. V. Kershaw, S. Kalytchuk, O. Tomanec, L. Jing, A. S. Sussha, R. Zboril, A. L. Rogach, *Nat. Commun.* **2017**, *8*, 996.
- [26] Q. A. Akkerman, G. Rainò, M. V. Kovalenko, L. Manna, *Nat. Mater.* **2018**, *17*, 394.
- [27] S. J. Yoon, K. G. Stamplecoskie, P. V. Kamat, *J. Phys. Chem. Lett.* **2016**, *7*, 1368.
- [28] Y. Fu, F. Meng, M. B. Rowley, B. J. Thompson, M. J. Shearer, D. Ma, R. J. Hamers, J. C. Wright, S. Jin, *J. Am. Chem. Soc.* **2015**, *137*, 5810.
- [29] H. Lee, S. M. Dellatore, W. M. Miller, P. B. Messersmith, *Science* **2007**, *318*, 426.
- [30] S. Hong, J. Kim, Y. S. Na, J. Park, S. Kim, K. Singha, G. Im, D. Han, W. J. Kim, H. Lee, *Angew. Chem., Int. Ed.* **2013**, *52*, 9187.
- [31] S. I. A. Cohen, M. Vendruscolo, M. E. Welland, C. M. Dobson, E. M. Terentjev, T. P. J. Knowles, *J. Chem. Phys.* **2011**, *135*, 065105.
- [32] M. D'Ischia, A. Napolitano, A. Pezzella, P. Meredith, T. Sarna, *Angew. Chem., Int. Ed.* **2009**, *48*, 3914.
- [33] G. Loget, J. B. Wood, K. Cho, A. R. Halpern, R. M. Corn, *Anal. Chem.* **2013**, *85*, 9991.
- [34] Y. Liu, K. Ai, L. Lu, *Chem. Rev.* **2014**, *114*, 5057.
- [35] Y. Lin, L. Shen, J. Dai, Y. Deng, Y. Wu, Y. Bai, X. Zheng, J. Wang, Y. Fang, H. Wei, *Adv. Mater.* **2017**, *29*, 1604545.
- [36] Y. Shao, Z. Xiao, C. Bi, Y. Yuan, J. Huang, *Nat. Commun.* **2014**, *5*, 5784.
- [37] S. M. Vorpahl, S. D. Stranks, H. Nagaoka, G. E. Eperon, M. E. Ziffer, H. J. Snaith, D. S. Ginger, *Science* **2015**, *348*, 683.
- [38] H. Zhang, Y. Wu, C. Shen, E. Li, C. Yan, W. Zhang, H. Tian, L. Han, W. Zhu, *Adv. Energy Mater.* **2019**, *9*, 1803573.
- [39] S. G. Motti, D. Meggiolaro, A. J. Barker, E. Mosconi, C. A. R. Perini, J. M. Ball, M. Gandini, M. Kim, F. De Angelis, A. Petrozza, *Nat. Photonics* **2019**, *13*, 532.
- [40] B. R. Sutherland, E. H. Sargent, *Nat. Photonics* **2016**, *10*, 295.
- [41] M. Karaliūnas, E. Kuokštis, K. Kazlauskas, S. Juršėnas, V. Hoffman, A. Knauer, in *Sixth Int. Conf. on Advanced Optical. Materials and Devices*, SPIE, Bellingham, WA **2008**, p. 71420U.
- [42] S. Delikanli, F. Isik, F. Shabani, H. D. Baruj, N. Taghipour, H. V. Demir, *Adv. Opt. Mater.* **2021**, 2002220.
- [43] S. Cho, S. H. Yun, *Commun. Chem.* **2020**, *3*, 15.
- [44] L. A. Morton, J. P. Saludes, H. Yin, *J. Vis. Exp.* **2012**, *64*, e4151.
- [45] M. Liu, T. Zentgraf, Y. Liu, G. Bartal, X. Zhang, *Nat. Nanotechnol.* **2010**, *5*, 570.
- [46] L. Dou, M. Lai, C. S. Kley, Y. Yang, C. G. Bischak, D. Zhang, S. W. Eaton, N. S. Ginsberg, P. Yang, *Proc. Natl. Acad. Sci. U.S.A.* **2017**, *114*, 7216.
- [47] S. F. Kingsmore, *Nat. Rev. Drug Discovery* **2006**, *5*, 310.
- [48] T. Ha, P. Tinnefeld, *Annu. Rev. Phys. Chem.* **2012**, *63*, 595.
- [49] S. J. J. Kwok, N. Martino, P. H. Dannenberg, S.-H. Yun, *Light Sci. Appl.* **2019**, *8*, 74.
- [50] T. Xia, M. Kovichich, M. Liang, H. Meng, S. Kabehie, S. George, J. I. Zink, A. E. Nel, *ACS Nano* **2009**, *3*, 3273.
- [51] T. S. Sileika, D. G. Barrett, R. Zhang, K. H. A. Lau, P. B. Messersmith, *Angew. Chem., Int. Ed.* **2013**, *52*, 10766.